Materials Research. 2025; 28:e20240276
DOI: https://doi.org/10.1590/1980-5373-MR-2024-0276

Microstructural Evolution of UNS S32205 Duplex Stainless Steel During Cold Rolling and Subsequent Annealing

C. Gauss[a,b]*, *M.J.R. Sandim*[a], *H.R.Z. Sandim*[a]

[a]*Universidade de São Paulo, Escola de Engenharia de Lorena,12602-810, Lorena, SP, Brasil.*
[b]*University of Waikato, School of Engineering, 3240, Hamilton, New Zealand.*

Received: June 25, 2024; Revised: October 08, 2024; Accepted: December 01, 2024

We followed the microstructural evolution of UNS S32205 duplex stainless steel during cold rolling up to 79% reduction in thickness and at early stages of isothermal annealing at 1080ºC. Qualitative analysis of peak broadening and kernel average misorientation (KAM) parameter obtained by X-ray diffraction (XRD) and electron backscatter diffraction (EBSD), respectively, indicated a higher work hardening of austenite. Strain-induced martensite was not detected within this strain range by using X-ray diffraction and DC-magnetisation measurements. Two particular rolling thickness reductions were chosen for recrystallisation studies; i.e., 43% and 64%. After annealing for 1 min, primary recrystallisation occurred in ferrite (42% of recrystallised grains for 43% cold rolling), whereas austenite only recovered. For a reduction of 64%, the recrystallised fraction of ferrite did not change significantly, while austenite reached a recrystallised fraction of 43%. Full recrystallisation is noticed after annealing for 3 min for both conditions resulting in a bamboo-like grain structure.

Keywords: *Duplex stainless steel, UNS S32205, Peak broadening analysis, Recrystallisation, Texture, EBSD.*

1. Introduction

Duplex stainless steels (DSS) have increasingly been used in applications that demand high mechanical strength, high toughness and good corrosion resistance, mainly in the chemical, petrochemical, oil and gas, nuclear, and pulp and paper industries[1-4]. These properties are possible due to a layered two-phase microstructure formed by approximately equal fractions of austenite (γ) and ferrite (α). Ferrite provides high mechanical strength and austenite yields ductility and uniform corrosion resistance[5,6]. These steels solidify into a ferritic structure, while austenite forms in the solid state. During hot rolling, layers of ferrite and austenite alternate due to the low interfacial energy associated with these two phases[1,7].

The alternate layers of ferrite and austenite (lamellar structure) significantly affect the deformation behaviour of duplex stainless steels. The acting deformation mechanism (dislocation slip or twinning) is strongly dependant on the stacking fault energy (SFE) in face-centred cubic (FCC) metals and alloys. Dislocation slip occurs in metals with medium to high SFE while mechanical twining is an alternative deformation mechanism for FCC metals with low SFE or when deformation occurs at very low temperatures[8]. While the FCC structure of austenite has a lower number of slip systems, the orientation and activation of these slip planes are generally more favourable than in the body-centred cubic (BCC) structure of ferrite, especially at room temperature. This typically results in higher ductility in austenite. However, as plastic deformation occurs, austenite accumulates more dislocations than ferrite to maintain strain compatibility between the phases. In addition to dislocation slip, mechanical twinning and strain-induced martensite (SIM) formation are commonly observed in low-SFE austenite during deformation, further contributing to its complex deformation mechanisms[1,9-11].

The anisotropy in the mechanical properties of cold-rolled duplex stainless steels, an important parameter to be considered in several applications, is not only related to the effect of the morphology of its two-phase structure. The crystallographic texture of the constituent phases directly affects their properties, becoming an important characteristic considering that cold rolling is present in several stages of their manufacture[12,13]. The evolution of the crystallographic texture during plastic deformation of duplex stainless steels differs from that of single-phase stainless steels due to the lamellar morphology of the two-phase structure and the mechanical interaction between the phases. This peculiar structure reduces lattice rotations and influences the plastic deformation behaviour of both phases, promoting the appearance of certain texture components and the absence or lower intensity of some components characteristic in ferritic and austenitic single-phase stainless steels[14-17]. In addition to chemical composition (SFE), the effects of texture and grain morphology can favour or hinder the stability of austenite for the formation of SIM in duplex stainless steels[18].

In the annealing of cold-rolled duplex stainless steels, important microstructural changes are observed, considering the dependence of the strain difference between the phases

*e-mail: christian.gauss@waikato.ac.nz

on the relative volume fraction, size, and strength of each phase[8]. Dislocation distribution in the deformed state and recrystallisation mechanisms differ from one phase to another. During annealing, ferrite undergoes static recovery before the onset of recrystallisation, while austenite recovers to a much lesser extent. Although ferrite undergoes a decrease in driving force for recrystallisation due to recovery, it has faster recrystallisation kinetics and begins at lower temperatures[19,20].

Studies related to plastic deformation, texture, phase transformation (precipitation), and recrystallisation are of technological importance, given that these concurrent phenomena are present in all manufacturing stages of duplex stainless steels[21,22]. Several works address how microstructural evolution and deformation compatibility between ferrite and austenite occur in cold-rolled DSSs[23-31]. Among them, some focus on the specific UNS32205 grade[11,24,30,31]. In this context, Kumar et al.[30,31] reported solely on deformation behaviour, while Malta *et al*. reported on recrystallisation aspects for this steel grade[24]. In the latter work, the authors used electron backscatter diffraction (EBSD) to follow microstructure and texture evolution in a steel with a 75% thickness reduction, annealed at 900°C and 1100°C for 180 s. However, despite these important contributions, a comprehensive understanding of the interplay between deformation, phase transformation, and recrystallisation under different thermomechanical conditions in duplex stainless steels remains limited, necessitating further investigation.

In this work, we conducted a comprehensive assessment of the microstructural changes of a standard UNS32205 DSS after cold rolling and subsequent annealing using EBSD, X-ray diffraction (XRD), and magnetisation measurements. The strain partitioning, crystallographic microtexture of each phase, and possible formation of SIM in austenite after cold deformation were investigated. Additionally, the mechanisms involved in the initial stages of recovery and recrystallisation of each phase at 1080°C were elucidated through grain orientation spread (GOS) and texture analyses.

2. Materials and Methods

The investigated material in this work was a hot-rolled UNS S32205 duplex steel, homogenised at 1080ºC. The full chemical composition is shown in Table 1. The steel was supplied as a 5-mm thick plate and cold rolled (room temperature) in multiple passes to 23, 43, 64, and 79% of thickness reduction (named S23, S43, S64, and S79 henceforth), corresponding to a true strain (ε) of up to 1.56. For the recrystallisation study, small samples of 5 x 5 x t mm^3 were extracted from the plates with intermediate thickness reductions (S43 and S64) and annealed in air at 1080°C for 1, 3, 5 and 7 min followed by cooling in ice water. The chemical composition of each phase in the as-received material was determined via EDS (Energy-Dispersive X-ray Spectroscopy) using a Swift ED3000 from Oxford Instruments coupled to a Hitachi benchtop scanning electron microscope model TM3030.

Table 1. Chemical composition of the studied UNS S32205 duplex stainless steel. Contents are given in mass%.

C	Mn	Si	P	S	Cr
0.0199	1.83	0.33	0.0284	0.0002	22.6
Ni	Mo	Al	Cu	N	O
5.37	3.03	0.0041	0.216	0.1484	0.0024

EBSD maps for the longitudinal section (RD x ND) of the samples were obtained using a Zeiss Merlin scanning electron microscope operating with an accelerating voltage of 20 kV coupled with an Edax Hikari EBSD camera. Metallographic preparation included grinding with a #1200 SiC paper and polishing using diamond suspensions of 9 µm, 6 µm, 3 µm, and 1 µm followed by final polishing with a 0.3 µm-alumina slurry. Electrolytic etching was used for the last polishing step using H_2SO_4 solution of 20% (v/v) in CH_3OH at a constant voltage of 12 V for 15 s. High-resolution EBSD maps were acquired with step sizes of 40 and 30 nm. This last step size was used for the most deformed samples (S64 and S79). Standard EBSD data clean-up procedures were adopted and all pixels with confidence index lower than 0.1 were removed from the maps. Texture was evaluated from the EBSD data based on orientation distribution functions (ODFs) using the discrete binning method and Bunge notation. From the EBSD maps, both GOS (grain orientation spread) and KAM (kernel average misorientation) parameters were also evaluated. GOS is defined as the average difference between the average orientation of a grain and all individual orientations within this grain[32]. This parameter is used to distinguish between recrystallised and deformed grains, where higher GOS values are found in deformed grains. Grains are considered recrystallised when they have GOS values below 1º-3º, depending on the material[33–35]. In this work, grains with GOS < 1º are considered recrystallised.

KAM is defined as the average misorientation around a pixel with respect to a defined set of nearest pixels[36]. This parameter is used for the evaluation of local plastic strain and is associated with dislocation density[37]. In this work, KAM was calculated up to the sixth and eighth neighbours for the obtained maps using step sizes of 40 and 30 nm, respectively. In both cases, the maximum misorientation angle considered was 5º. All EBSD data were processed using the EDAX TSL OIM software (version 7.1).

For the XRD analysis, 20 x 20 mm^2 specimens were cut from the as-received and cold-rolled samples and ground up to half of the thickness. The surface was then ground with SiC papers (#800, #1000, and #2400) and polished using a colloidal silica suspension of 0.04 µm. The final polishing was conducted through electrolytic etching with a perchloric acid solution in water and ethanol (5% v/v) at a constant voltage of 16 V for 60 s using a cathode made of stainless steel. XRD experiments were performed in a Panalytical diffractometer, using a Cu-Kα radiation (40 kV, 30 mA) with a Ni-filter, in the range of $10º \leq 2\theta \leq 120º$ with a step of 0.01º and counting time of 100 s. The data were analysed using the software Panalytical HighScore Plus©. From the diffraction data, the estimation of the volume fraction of the phases present in the deformed material was made using the direct comparison method. According to this method, the integrated intensity of all reflections of each phase is proportional to its volume fraction[38].

Peak broadening analysis from X-ray data is useful to obtain information about the microstructure. Besides instrumental effects, peak broadening is affected by changes in both crystallite size and lattice distortions (microstrain)[38].

Considering plastic deformation to large strains, it is reasonable to assume that the peak broadening comes from the microstrain. Based on this, the estimation of microstrain <ε> for the deformed material was made using the Stokes formula[39]:

$$\epsilon = \frac{\beta_d(2\theta)}{4\tan\theta} \quad (1)$$

where $\beta_d(2\theta)$ is the integral width in radians for a given (h k l) plane and θ is the peak position. The integral width is defined as the width of a rectangle of the same height and area of the analysed peak. The instrumental broadening from the XRD instrument was subtracted from all the measurements using a crystalline silicon standard.

The microstructural characterisation of the material was complemented with Vickers microhardness testing of each phase using a load of 5 g for 12 s (Clemex model MMT). The phases were identified through electrolytic etching using an aqueous solution of NaOH 20% m/V. The annealed samples were also characterised by light optical microscopy using a Zeiss AxioVert microscope. The surface of the samples was ground with SiC papers (#800, #1000, and #2400), polished using a colloidal silica suspension of 0.04 μm followed by electrolytic etching with a nitric acid aqueous solution (40% v/v) at voltages between 1.2-1.5 V for 30-60 s using a stainless-steel cathode. This electrolytic etching is used to reveal grain boundaries and selectively reveal ferrite. Thermodynamic calculations were performed using the Thermo-Calc© software with TCFE7 database using the steel chemical composition given in Table 1 as input data.

For DC-magnetic characterisation, samples with dimensions of 1 x 1 x 5 mm^3 were cut from the centre of each plate (as-received and cold-rolled plates), keeping the largest dimension parallel to the rolling direction and the applied magnetic field. For thicknesses greater than 1 mm, samples were taken from half the thickness. For each condition, three samples were prepared. DC-magnetisation (M) as a function of applied field (H) curves (hysteresis loops) were obtained for an H of up to 20 kOe (25°C). The number of points collected varied with the applied field. In the range of 20 to 5 kOe, the total number of points collected was 15. From 5 to 0.5 kOe, 25 points were collected. From 0.5 to -0.5 kOe (inversion in the direction of the applied field) the total number of points collected was 25. This methodology was used to better define the curves for determining the coercive field (H_c). The measurements were performed using a Vibrating Sample Magnetometer (VSM) from EG&G Princeton Applied Research. From hysteresis loops, the saturation magnetisation (M_s) and the coercive field (H_c) were obtained with an accuracy of 2% of the measured value and ± 5 Oe, respectively.

3. Results and Discussion

3.1. As-received material

Figures 1a, b show the image quality (IQ) combined with phase maps for the as-received material and a map of high (HAB) and low (LAB) angle boundaries. In this condition, the microstructure consists of alternating lamellae of ferrite and austenite (red and green respectively) but presents a

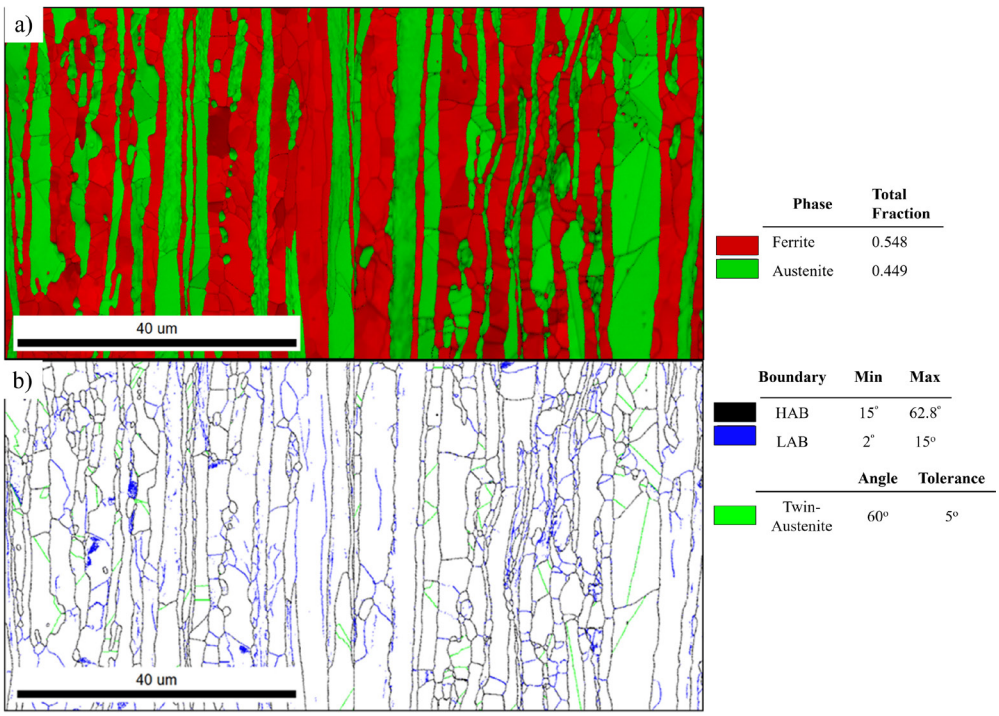

Figure 1. a) Phase map overlaid with image quality map obtained by EBSD analysis of the as-received material. Ferrite is represented in red and austenite in green. b) Boundary distribution map obtained by EBSD analysis of the as-received material. In this map, low (blue) and high angle (black) boundaries of both phases as well as twin (green) boundaries of austenite are shown.

heterogeneous distribution in relation to the morphology of the lamellae. According to this map, the ferrite fraction in the as-received material is ~ 0.58. Despite the material's processing history, a large number of LAB (blue lines) are observed in relation to HAB (black lines). In austenite, the presence of annealing twins (green lines) is also noticeable within some grains. This large number of LABs (between 2 and 15°) indicates that the material is not fully recrystallised in the as-received condition.

Figures 2a, b show both GOS and KAM maps for austenite and ferrite phases in the as-received condition, respectively. From Figure 2b it is noted that only 6.6% of the ferritic grains can be considered recrystallised since they present GOS < 1º. Although most ferrite grains have a value of GOS > 1°, the KAM value is low for almost all of them, which means that they have low stored energy. Such features indicate that ferrite is recovered. The analysis of Figure 2a shows that, in comparison to ferrite, austenite has a higher fraction of grains with GOS < 1° (0.535). In this case, it is clearly noted that areas with GOS < 1° (recrystallised grains) have low KAM values while grains with GOS > 1° have higher KAM values. Although austenite presents a higher fraction of recrystallised grains, both phases present a microstructure inherited from thermomechanical processing. Therefore, solution annealing after hot rolling proved ineffective to achieve a 100% recrystallised microstructure in the investigated steel.

3.2. Cold-rolled condition

3.2.1. X-ray diffraction and hardness

Figure 3 shows the X-ray diffractograms obtained for as-received and deformed conditions with up to 79% of thickness reduction. No other phases were detected besides ferrite and austenite. From the comparison with the theoretical diffraction patterns, considering an amount of 50% of each phase (not shown), the (*hkl*) planes (002) and (112) for ferrite

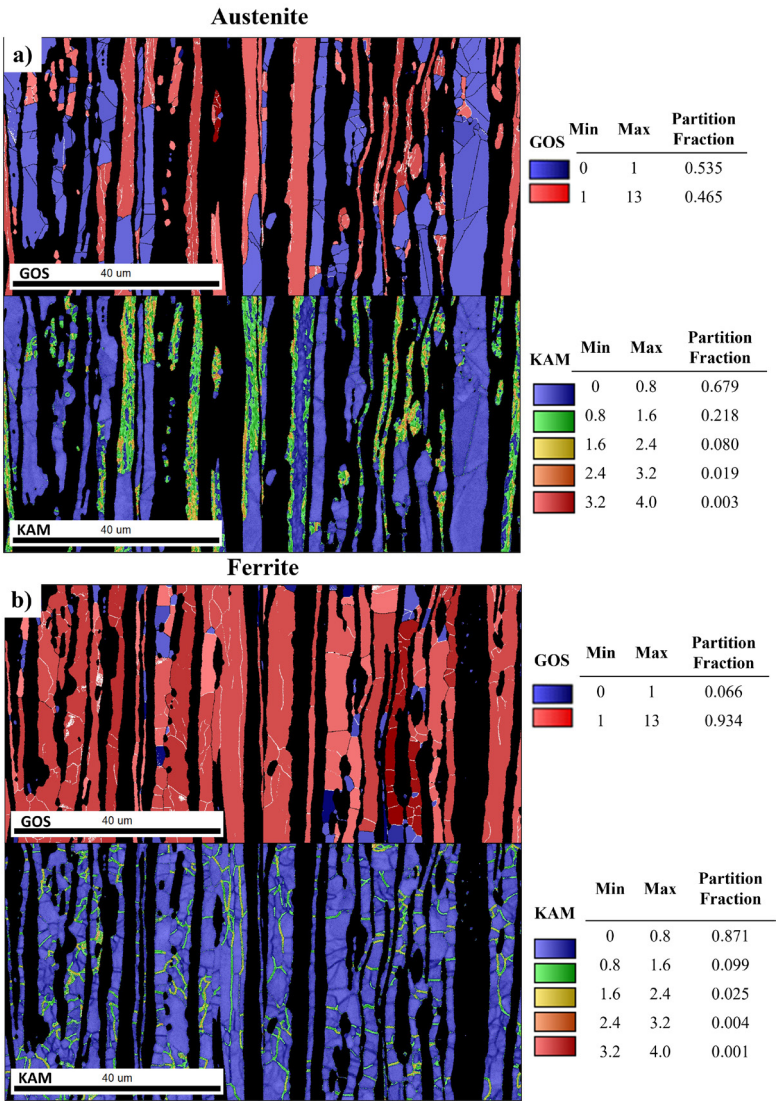

Figure 2. Comparison between GOS and KAM maps of austenite (a) and ferrite (b) in the as-received condition.

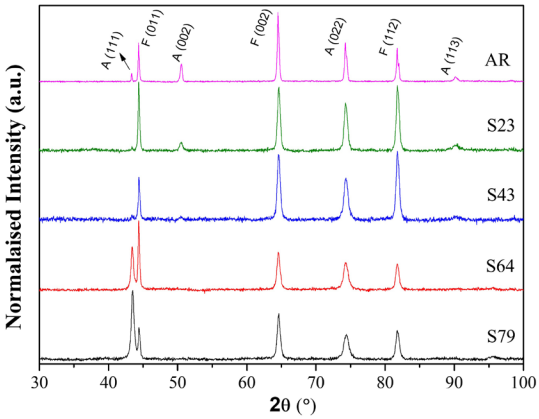

Figure 3. X-ray diffractograms of as-received (AR) and cold-rolled (thickness reductions of 23-79%) UNS S32205 duplex stainless steel.

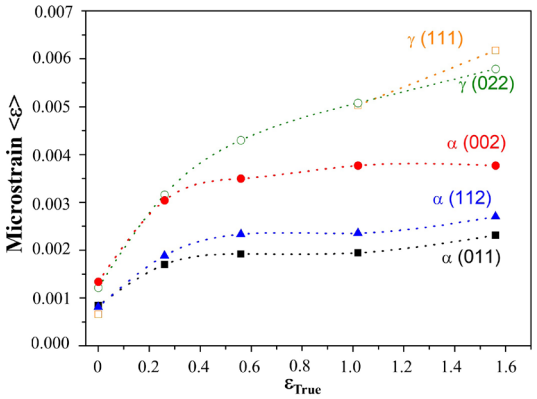

Figure 4. Changes in microstrain < e > as a function of true strain for austenite planes (022) and (111) and ferrite planes (112), (002), and (011).

and (220) for austenite were less affected by texture. For this reason, these sets of planes were used to determine the volume fractions of the phases using the direct comparison method. The results are given in Table 2. The total ferrite and austenite contents are unchanged with deformation, remaining close to 50% (minor deviations from this value are likely due to unavoidable texture effects).

To estimate the strain difference between ferrite and austenite, the microstrain was calculated according to Equation 1, using the (011), (112) and (002) planes of ferrite and (111) and (022) planes of austenite. The microstrain is directly associated with the degree of crystal lattice distortion caused by plastic deformation. Therefore, it is expected that higher values are associated with a more pronounced work hardening. The results of microstrain as a function of true strain are displayed in Figure 4. For high strain levels, there is a higher increase of microstrain in austenite than in ferrite. Such feature is corroborated by the results displayed in Figure 5. This figure shows how hardness varies as a function of true strain for each phase individually. These measurements were performed on the RD-TD section of the deformed material (i.e., the rolling plane), in which the phases have a coarser morphology. From these results, despite the similar behaviour, austenite has higher work hardening than ferrite during cold rolling. Similar results were reported by Simon et al. in a X2CrNiN23-4 DSS and Breda et al. in a UNS S32205 DSS, both of which evaluated the strain partitioning between ferrite and austenite[11,40].

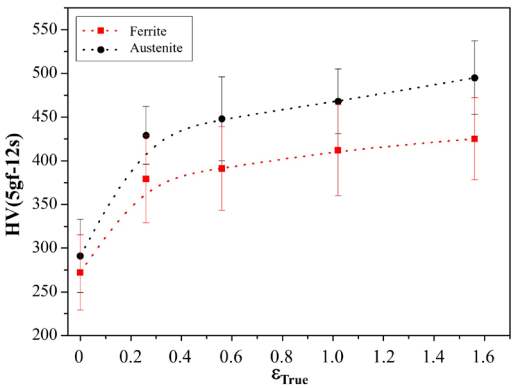

Figure 5. Strain hardening curves for austenite and ferrite in UNS S32205 duplex stainless steel.

Table 2. Results of phase quantification from XRD data.

Phase fraction - XRD			
Thickness reduction (%)	True strain	Austenite	Ferrite
0	0	0.42	0.58
23	0.26	0.45	0.55
43	0.56	0.47	0.53
64	1.02	0.53	0.47
79	1.56	0.51	0.49

3.2.2. DC-magnetisation

In duplex stainless steels, the FCC phase is paramagnetic, while the BCC (ferrite or α'-martensite) phase is ferromagnetic. Therefore, bulk magnetisation measurements are very useful to evaluate the likely formation of strain-induced martensite in this particular class of materials, if any. For this purpose, the most used magnetic parameter is saturation magnetisation (M_s), which is related to the volume fraction of ferromagnetic phases in the material[41]. In addition, the coercive field (H_c), which mirrors the strength of pinning for the magnetic domain walls[41] is also sensitive to the presence of strain-induced martensite in the material. On one hand, for ferritic steels, H_c is dependent on grain size (D) and dislocation density (ρ), so that[42]:

$$H_c \propto 1/D \quad (2)$$

$$H_c \propto \sqrt{\rho} \quad (3)$$

On the other hand, for austenitic stainless steels, H_c is directly related to the density of the interfaces between α'-martensite and austenite [43]. When the size of α'-martensite clusters is small (regime of low plastic deformation), the coercivity increases with strain. However, for high deformation, if the volume fraction of α'-martensite is high, H_c decreases with strain[43]. For the stainless duplex steel, both ferrite and α'-martensite contribute to the overall behaviour of H_c[44].

Figure 6 shows representative magnetisation curves of the as-received and cold-rolled samples. The inset shows the central part of the hysteresis loops with higher magnification, for better visualization of the coercive field. Figure 7 shows the variation of the average M_s and H_c with strain, obtained for a set of three samples for each condition. Although there is a small increase in M_s for a true strain > 0.5, the M_s value for the highest strain is practically the same as for the as-received material. Considering the uncertainty of the measurements, the magnetisation analysis shows that there was not an increase in the fraction of the ferromagnetic phase. Consequently, SIM was not formed under the rolling conditions used in this study (or the volume fraction of SIM is below the detection limit of the technique). This finding aligns well with the conclusions drawn from the XRD data (Table 2). The gradual increase of the coercive field with strain, depicted in Figure 7b, is attributed to the plastic deformation of ferrite, in agreement with Equation 3.

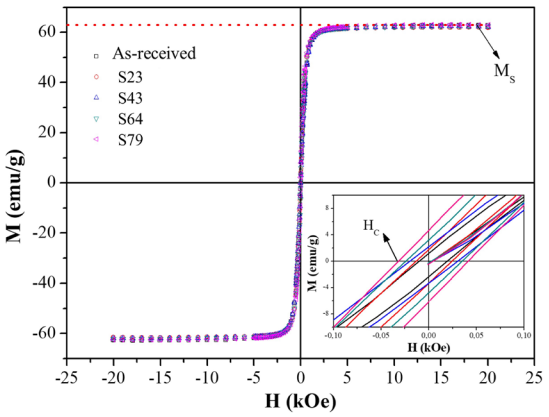

Figure 6. Magnetisation curv=es of UNS32205 DSS in as-received and cold-rolled conditions for thickness reductions of 23-79%. The coercive field (H_c) increases with cold rolling strain as highlighted in the inset.

3.2.3. Estimations of Md_{30} and strain-induced martensite formation

Austenite stability is a key issue with regard to the possibility of SIM formation in duplex stainless steels. Md_{30}, i.e., the temperature at which 50 vol% α'-martensite forms at a true tensile strain of 0.3 in metastable austenitic steels is a good and common predictor reported in the literature[45]. Md_{30} was calculated using Equation 4 (each atomic symbol represents the mass% of the corresponding element) for three different conditions assuming: *i)* the global chemical composition of the steel; *ii)* the chemical composition of the austenite calculated from thermodynamic calculations (CALPHAD method) at 1080°C where equal fractions of austenite and ferrite coexist; *iii)* the chemical composition of the austenite determined from EDS measurements in SEM (Table 3).

$$Md_{30}(K) = 824 - 462(C+N) - 9.2Si - 8.1Mn - 13.7Cr - 29.0(Ni+Cu) - 18.5Mo - 68.0Nb \quad (4)$$

In a recent paper, Masumura *et al.* revisited classical empirical equations to estimate Md_{30} in austenite[46]. According to the authors, previous empirical equations underestimate the effects of carbon and nitrogen on the stability of austenite. They proposed a new equation based on multiple regression analysis for carbon and nitrogen coefficients, as shown in Equation 5:

$$Md_{30}(K) = 756 - 555C - 528N - 10.3Si - 12.5Mn - 10.5Cr - 24.0Ni - 5.6Mo \quad (5)$$

The initial result of Md_{30} = 200.9 K, which is based on the global composition, is the least realistic, as it does not account for the partitioning of alloying elements. Given that EDS-SEM is not the most accurate technique to determine the content of low-Z interstitial elements, such as carbon and nitrogen, the value given by the CALPHAD method gives Md_{30} = 139.5 K (-133.7°C), well below the temperature where rolling was carried out (room temperature). The Md_{30}

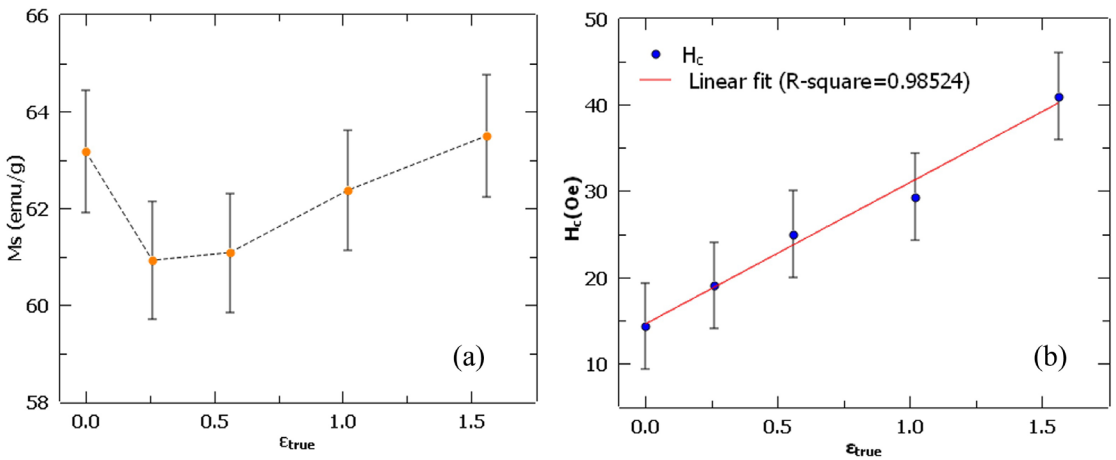

Figure 7. Saturation magnetisation (a) and coercive field (b) plots in relation to true strain. Each point corresponds to the average of three samples.

Table 3. Thermo-Calc® (TC) thermodynamic calculations and experimental results of austenite chemical composition (EDS-SEM) and Md_{30} temperature (given in K) calculated using Equations 4 and 5 for UNS S32205 duplex stainless steel. Contents are given in mass%.

Method	Md_{30} (4)	Md_{30} (5)	C	N	Si	Mn	Cr	Ni	Cu	Mo
Global (Aperam)	200.9	257.3	0.020	0.148	0.330	1.83	22.6	5.37	0.216	3.03
Austenite (TC)	139.5	178.9	0.035	0.263	0.300	2.09	20.4	6.77	0.275	2.37
Austenite (SEM)	176.4	233.0	0.020*	0.148*	0.440 ±0.044	2.05 ±0.112	22.0 ±0.154	6.54 ±0.177	0.216*	2.80 ±0.147

*Elements not measured by EDS-SEM. Values of global composition used instead.

estimated from Equation 5 using the chemical composition obtained by thermodynamic calculations shown in Table 3 is equal to 178.9 K (-98.1°C). The Md_{30} values indicate that the formation of SIM at room temperature is very unlikely for this steel grade, which is supported by the measurements of DC-magnetisation and XRD.

Malta et al.[24] reported the formation of SIM in a similar cold-rolled UNS S32205 steel deformed to 75% reduction based on EBSD image quality maps; however, this amount has not been quantified either using XRD or bulk magnetisation techniques. It is noteworthy that orientation effects can affect image quality maps, as some orientations have high-intensity diffraction patterns while others do not[47].

The occurrence of SIM in UNS S32205 steel has also been reported by Breda et al.. However, the authors noted that, despite the austenite in duplex stainless steel having a lower stacking fault energy (SFE), it is more stable than in single-phase stainless steels, such as 304L[11]. They observed slower SIM transformation kinetics and a lower amount of SIM compared to 304L stainless steel. This was mainly attributed to the biphasic structure of DSS, which imposes deformation constraints that affect the development of microstructural features due to phase interactions. By comparing the UNS S32205 grade with other DSS grades, such as UNS S32101 and UNS S32304, Breda et al.[18] also reported improved austenite stability after significant deformation, particularly in terms of SIM formation. Furthermore, these authors observed minimal variation in the saturation magnetic flux density (as determined by DC magnetisation measurements) for UNS S32205 and UNS S32507 DSS grades, even with thickness reductions of up to 85%.

3.2.4. EBSD

Figure 8 shows the combination of phase and image quality (IQ) maps from EBSD data for as-received and deformed conditions (up to 79% thickness reduction). Most of the darker regions (low IQ values) belong to austenite. Shear bands, making an angle of about 35° in relation to the RD, are seen for the most deformed samples (see Figures 8d, e), most markedly in austenite. The extension of these shear bands seems to be limited to the individual lamellae due to the phase boundaries. In single-phase materials, shear bands cross several grains and have much larger dimensions than those found in the investigated samples[48].

Based on the EBSD maps displayed in Figure 8, the corresponding KAM distributions as a function of deformation were obtained for both phases, as shown in Figures 9a, b. In the as-received material (Figure 9a), ferrite and austenite present recovered and partly-recrystallised microstructures, respectively. Consequently, in this condition, for both phases, low KAM values predominate. With increasing strain, despite a considerable increase in the fractions of higher KAM values in both phases, it can be seen that these fractions are greater in austenite than in ferrite. Such feature can be better visualized in Figure 9b, which compares the mean values of KAM parameter as a function of deformation for both phases. As higher KAM values are mainly related to a higher dislocation density, the results displayed in Figure 9 also indicate that the more pronounced hardening occurs in austenite than in ferrite.

Regarding texture, Figure 10 depicts the representative sections of ODFs plots for ferrite and austenite phases in the as-received and S79 sample. In the as-received condition, both phases exhibit a strong texture. In ferrite, the texture components belonging to α (<011>//RD) and γ (<111>//ND) fibres are visualized with greater intensity and, to a lesser extent, the {001}<110> Rotated Cube component.

In austenite, the {001}<100> Cube, {123}<634> S, and {011}<211> Brass texture components are present, the latter being the most intense. The {011}<211> and {001}<110> components found in austenite and ferrite, respectively, are typical deformation texture components, although the analysed material in the as-received condition was hot rolled and annealed after rolling. For the cold-rolled material, austenite shows a weakening of the {112}<111> Copper and {001}<100> Cube components, accompanied by a strengthening of the α-fibre ({011}<100> Goss- {011}<211> Brass). In ferrite, under cold rolling, there was the strengthening of the γ-fibre and {001}<110> Rotated Cube component as well.

3.3. Isothermal annealing and recrystallisation

Figure 11 shows the calculated equilibrium phase diagram of the investigated UNS S32205 duplex steel. According to this diagram, equal amounts of austenite and ferrite are found at 1080°C and there is no formation of other detrimental phases at this temperature. Because of these reasons, this temperature was chosen to evaluate the stability of the microstructure during isothermal annealing. Figure 12 shows the evolution of hardness as a function of annealing time at 1080°C, for both cold-rolling strains. For both reductions, there is a noticeable drop in hardness for annealing up to 3 min. Thereafter, no significant change in hardness is observed until 7 min of annealing time and the softening curve levels off. The sharp softening experienced

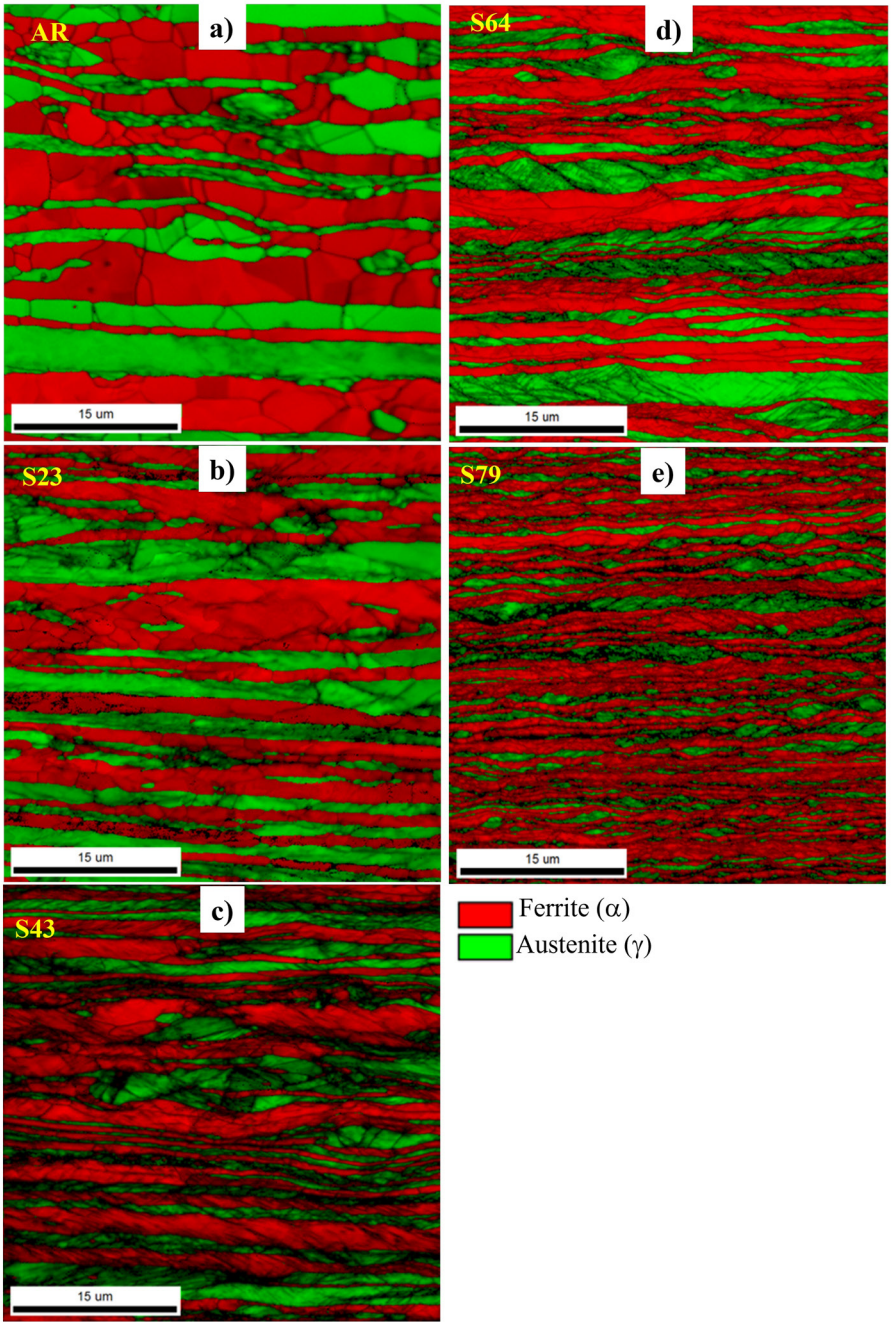

Figure 8. Phase maps overlaid with image quality map (gray lines) obtained by EBSD analysis of as-received (a) and cold-rolled samples (b-e).

by both phases is associated with static recovery and recrystallisation restoration reactions. Such feature is better observed in Figure 13, which shows the evolution of the microstructure of the S43 sample annealed at 1080°C. After annealing for 3 min, the microstructure is almost fully recrystallised and develops a bamboo-like grain structure with alternating layers of ferrite and austenite, which remains unchanged until the maximum annealing time investigated. Such morphology is more intense for the annealed material with higher deformation (not shown).

To better understand the mechanisms acting at the beginning of recrystallisation, Figure 14a shows the combination of the phase and image quality maps for samples S43 and S64 annealed at 1080°C for 1 min. From these maps, the austenite in sample S43 still has a deformation microstructure (elongated and fragmented grains), while ferrite in both conditions shows clear signs of recovery and/or recrystallisation. At this annealing stage, recovered/recrystallised ferrite grains exhibit a high aspect ratio. For longer times, this characteristic becomes less evident as the bamboo-like structure develops.

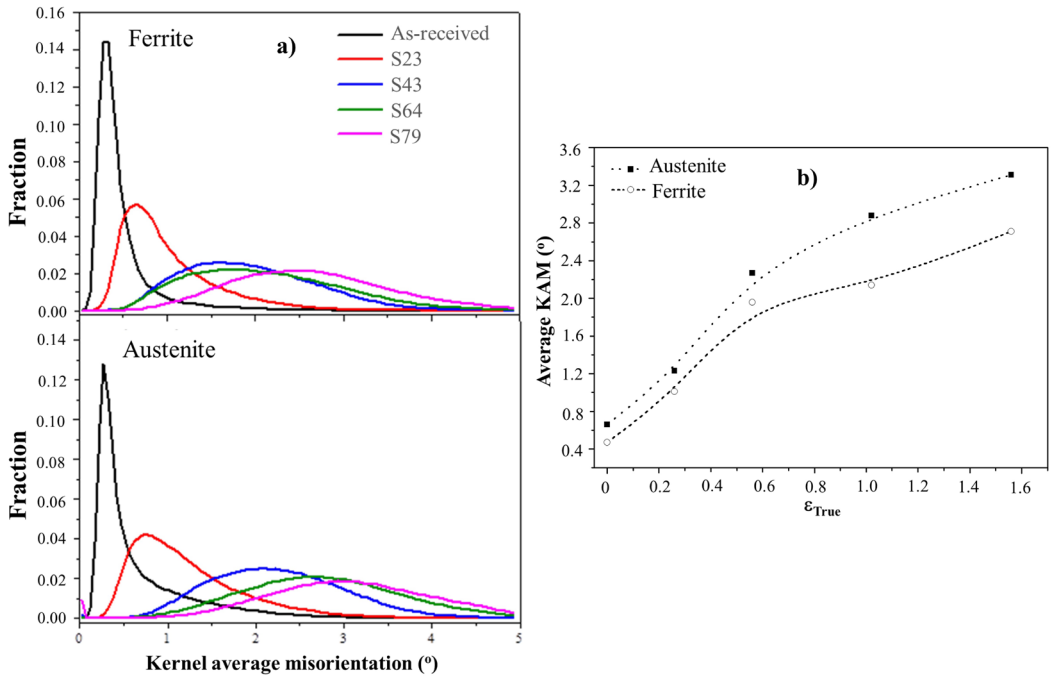

Figure 9. KAM distribution of ferrite and austenite in the as-received and cold-rolled conditions (a); Overall KAM distribution for ferrite and austenite as a function of true strain (b).

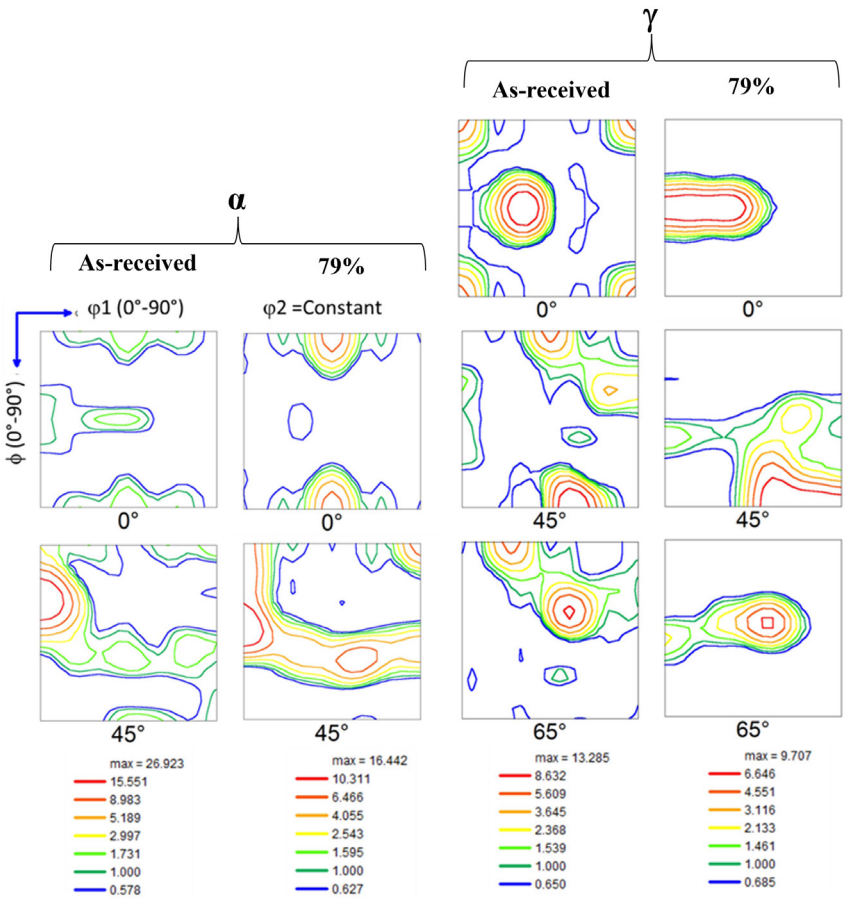

Figure 10. Orientation distribution function (ODF) of ferrite (α) and austenite (γ) in as-received and cold-rolled (S79) samples. Only representative constant φ_2 sections are shown for each phase.

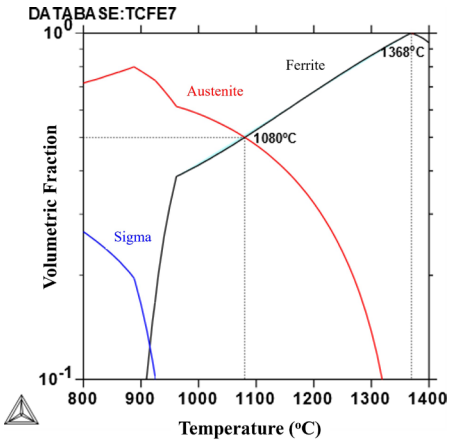

Figure 11. Equilibrium phase diagram of UNS S32205 duplex stainless steel. Equal amounts of austenite and ferrite are observed at 1080°C.

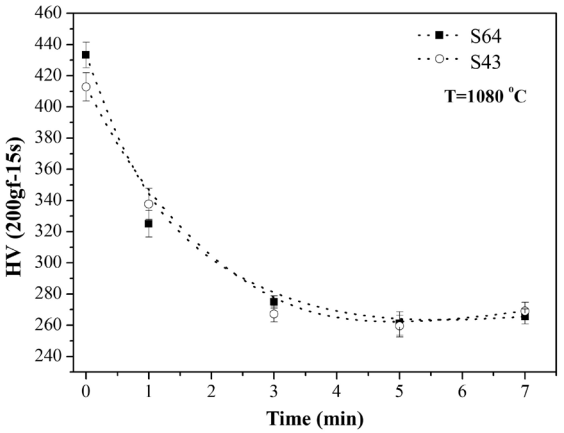

Figure 12. Softening behaviour at 1080°C of cold-rolled samples with 64% and 43% of thickness reduction.

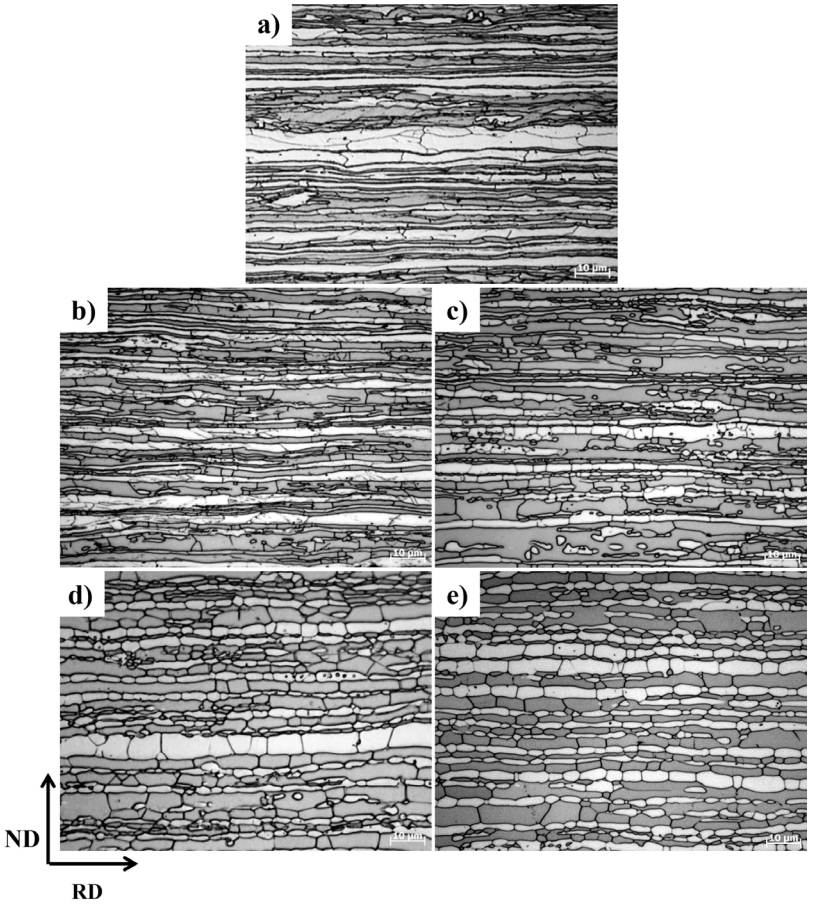

Figure 13. Light optical micrographs of UNS S32205 duplex stainless steel with 43% of thickness reduction (a) and annealed at 1080°C for 1 min (b), 3 min (c), 5 min (d), and 7 min (e).

Such features are better visualized in GOS maps displayed in Figure 14b. In these maps, the blue grains are considered recrystallised (GOS < 1°), while the red grains (GOS > 1°), are deformed or recovered. For sample S43, ferrite presented a fraction of 0.43 of recrystallised grains while austenite has a predominance of a fragmented microstructure with a high density of low angle boundaries (LAB). Regarding ferrite, it can be noted that the criteria of GOS < 1° is valid for both recovered and recrystallised grains. These elongated grains likely undergo static recovery since they maintain the same

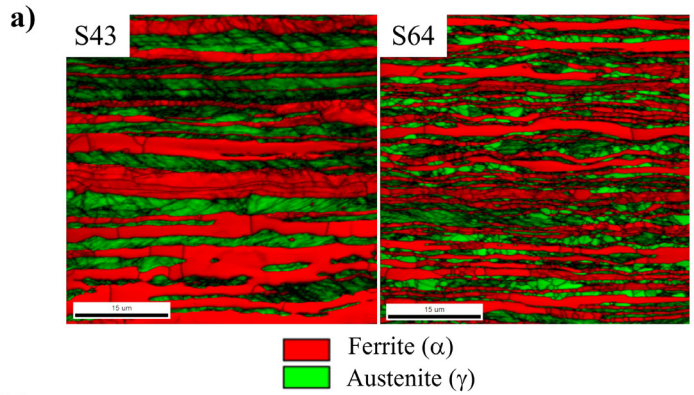

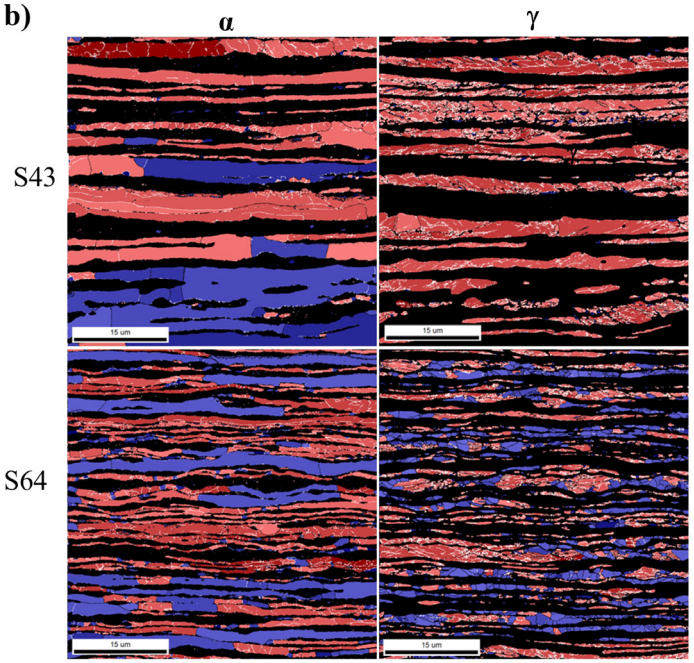

		Fraction			
	GOS (°)	S43-1min (Austenite)	S43-1min (Ferrite)	S64-1min (Austenite)	S64-1min (Ferrite)
	<1	0.020	0.424	0.429	0.442
	>1	0.980	0.575	0.570	0.558

Figure 14. (a) Phase map overlaid with image quality map, for samples S43 and S64 annealed at 1080°C for 1 min. (b) GOS maps of ferrite and austenite for samples S43 and S64 annealed at 1080°C for 1 min. Black lines mark the high angle, while white lines mark the low angle boundaries.

morphology inherited from the deformed state. The GOS < 1° criteria applies even for fragmented ferrite grains in sample S43 (Figure 14b). Both phases are partially recrystallised in sample S64, with fractions of recrystallised grains of 0.44 and 0.43 for ferrite and austenite, respectively.

Going further in the EBSD analysis, Figure 15 shows the KAM distributions for ferrite and austenite in both samples, in deformed and annealed states (1 min at 1080°C). After annealing, the KAM distribution shifts towards lower KAM values for both phases, as expected. In ferrite, the KAM distributions for both strains are similar, and the same behaviour is observed for the annealed conditions. For austenite, the KAM distribution tends to have higher values in the more deformed sample. This explains why there was no significant change in the recrystallised fraction of ferrite with increasing strain (S43 and S64). Contrastingly, a considerable difference was observed in austenite and higher KAM values are noticeable, indicating a greater driving force for discontinuous recrystallisation. Indeed, as seen in Figure 15, a noticeable increase in the fraction of low KAM values was observed in austenite, for annealed sample S64.

Regarding texture evolution with annealing, representative sections of the ODFs for ferrite and austenite phases in both deformed and annealed conditions for samples S43 and S64 are displayed in Figures 16a, b. No new texture components were observed in austenite after annealing for sample S43, which is in agreement with the fact that austenite is not found recrystallised in this sample (see Figure 16a). In ferrite, no

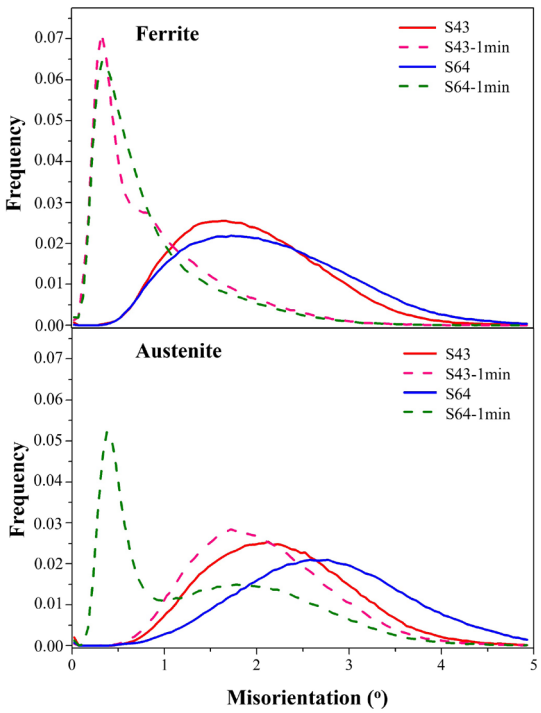

Figure 15. KAM distribution in ferrite (top) and austenite (bottom) of S43 and S64 samples annealed at 1080°C for 1 min.

strengthening of the γ-fibre was observed, but instead, both the α- and γ-fibres fragmented into individual texture components. For sample S64 (see Figure 16b), austenite shows a more pronounced change in texture under annealing compared to sample S43. In this case, there was a slight weakening in the {011}<110> Goss component and the appearance of a very weak {001}<100> Cube component, typical of recrystallisation in FCC metals. In ferrite, no major changes were observed in texture during annealing. Only a slight weakening of the γ-fibre and, as also observed in sample S43, a fragmentation of the fibre components. Our texture results are in agreement with those reported by Keichel et al.[20]. According to these authors, during recrystallisation, the development of specific texture components does not take place. Texture tends to become more random and some deformation components are maintained and/or fragmented.

This comprehensive set of results shows the absence of strain-induced martensite in austenite confirmed by XRD and magnetisation measurements, the differences in the work hardening behaviour of austenite and ferrite, and their subsequent annealing behaviour. These results are very useful in understanding how UNS S32205 duplex stainless steel deforms and recrystallises, with greater emphasis on the early stages of annealing where the bamboo-like grain structure develops.

4. Conclusions

The microstructural evolution of UNS S32205 duplex stainless steel during cold rolling up to 79% thickness reduction followed by isothermal annealing at 1080°C was investigated. The following conclusions can be drawn:

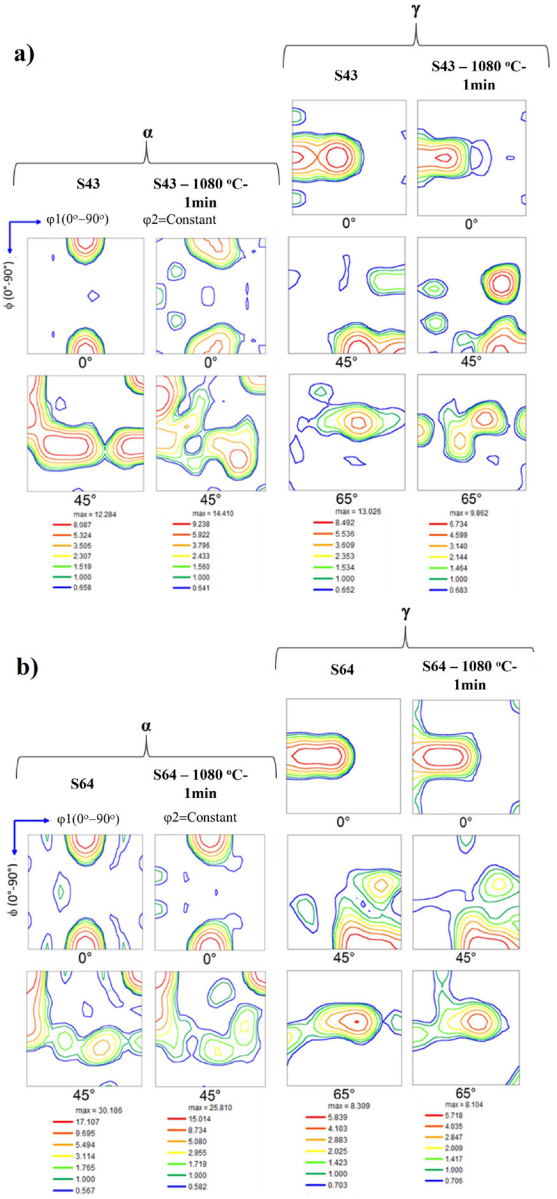

Figure 16. ODFs of a) cold-rolled S43 and b) S64 samples and corresponding annealed samples at 1080°C for 1 min. Only representative constant φ_2 sections are shown for each phase.

1. Solution annealing at 1080°C, used in the production of this steel, proved ineffective in promoting full recrystallisation of both phases in the as-received condition.
2. Strain-induced martensite was not detected by DC-magnetisation measurements in UNS S32205 duplex stainless steel, even at the highest thickness reduction achieved under the rolling conditions used in this study. This finding aligns well with the data obtained from X-ray diffraction and the Md_{30} estimation. The observed gradual increase in the coercive field with deformation is attributed to the plastic deformation of ferrite and the concurrent accumulation of lattice defects (dislocations and interfaces).

3. For S43 and S64 samples, the difference between their average values of KAM is larger for austenite. The same feature was observed for the microstrain determined from XRD measurements. For ferrite, such differences are quite small, which explains a slight increase in its recrystallisation fraction with the increase of the rolling strain;
4. Recrystallisation is completed after 7 min of annealing at 1080°C for the S79 sample. It begins in ferrite despite the greater fragmentation and hardening behaviour of austenite upon cold rolling. The recrystallised structure consists of alternating layers of ferrite and austenite and both phases develop a bamboo-like grain structure.
5. For austenite, the recrystallisation texture components are similar to those found in single-phase austenitic stainless steels. The cube component in austenite, typical of recrystallisation, is very weak. In ferrite, both α- and γ-fibres become fragmented after annealing at 1080°C for 1 min.

5. Acknowledgments

The authors are grateful to Aperam South America (Timóteo – MG) for supplying the steel used in this work and to Dr. J. Hoffmann from Karlsruher Institut für Technologie (KIT, Germany) for his support with EBSD measurements and to the Institute of Physics of the University of Sao Paulo (IF-USP, Brasil) for the DC-magnetisation measurements. CG thanks CAPES and KIT for his scholarship during the development of this work. HRZS is CNPq Fellow (National Council for Scientific and Technological Development, Brazil) under Grant no. 308.296/2021-4.

6. References

1. Lima NB, Lima LMFG, Reick W, Padilha AF. Deformation and recrystallization textures in duplex stainless steel. Mater Sci Forum. 2002;408-412:1353-8.
2. Miranda MAR, Sasaki JM, Tavares SSM, Abreu HFG, Neto JM. The use of X-ray diffraction, microscopy, and magnetic measurements for analysing microstructural features of a duplex stainless steel. Mater Charact. 2005;54(4-5):387-93.
3. Charles J. Duplex stainless steels: a review after DSS '07 held in grado. Rev Metall. 2008;105(3):155-71.
4. Francis R, Byrne G. Duplex stainless steels - alloys for the 21st century. Metals. 2021;11(5):836.
5. Weisbrodt-Reisch A, Brummer M, Hadler B, Wolbank B, Werner EA. Influence of temperature, cold deformation and a constant mechanical load on the microstructural stability of a nitrogen alloyed duplex stainless steel. Mater Sci Eng A. 2006;416(1-2):1-10.
6. Michalska J, Sozańska M. Qualitative and quantitative analysis of σ and χ phases in 2205 duplex stainless steel. Mater Charact. 2006;56(4-5):355-62.
7. Totten GE, editor. Steel heat treatment: metallurgy and technologies. Boca Raton: Taylor & Francis Group; 2006.
8. Humphreys FJ, Hatherly M. Recrystallization and related annealing phenomena. 2nd ed. USA: Elsevier; 2004.
9. Reick W, Pohl M, Padilha AF. Determination of stacking fault energy of austenite in a duplex stainless steel. Steel Res. 1996;67(6):253-6.
10. Lo KH, Shek CH, Lai JKL. Recent developments in stainless steels. Mater Sci Eng Rep. 2009;65(4-6):39-104.
11. Breda M, Brunelli K, Grazzi F, Scherillo A, Calliari I. Effects of cold rolling and strain-induced martensite formation in a SAF 2205 duplex stainless steel. Metall Mater Trans, A Phys Metall Mater Sci. 2015;46(2):577-86.
12. Hutchinson WB, Ushioda K, Runnsjö G. Anisotropy of tensile behaviour in a duplex stainless-steel sheet. Mater Sci Technol. 1985;1(9):728-36.
13. Ul-Haq A, Weiland H, Bunge H. Textures and microstructures in duplex stainless steel. Mater Sci Technol. 1994;10(4):289-98.
14. Rys J, Ratuszek W, Witkowska M. Comparison of the rolling texture formation of duplex with different initial texture. Arch Metall Mater. 2006;51(3):496-502.
15. Ryś J, Ratuszek W. Rolling texture formation in super-duplex stainless steel. Diffus Defect Data Solid State Data Pt B Solid State Phenom. 2010;163:145-50.
16. Rys J, Witkowska M. Rolling texture development in nitrogen alloyed ferritic-austenitic steel of duplex type. Arch Metall Mater. 2008;53(1):221-8.
17. Jura J, Baudin T, Mathon MH, Swiatnicki W, Penelle R. Microstructure and texture analysis in a cold-rolled austenitic-ferritic steel with duplex structure. Mater Sci Forum. 2002;408-412:1359-64.
18. Breda M, Ramous E, Almanza E, Calliari I. Strain-induced martensite detection methods in cold-rolled duplex stainless steels. Matls Perf Charact. 2017;6(3):MPC20160065.
19. Reick W, Pohl M, Padilha AF. Recrystallization and related phenomena. recrystallization-transformation combined reactions during annealing of a cold rolled ferritic-austenitic duplex stainless steel. ISIJ Int. 1998;38(6):567-71.
20. Keichel J, Gottstein G, Foct J. Recrystallisation in high nitrogen alloyed super duplex stainless steel. MSF. 1999;318-320:785-92.
21. Fargas G, Akdut N, Anglada M, Mateo A. Microstructural evolution during industrial rolling of a duplex stainless steel. ISIJ Int. 2008;48(11):1596-602.
22. Fargas G, Akdut N, Anglada M, Mateo A. Reduction of anisotropy in cold-rolled duplex stainless-steel sheets by using sigma phase transformation. Metall Mater Trans, A Phys Metall Mater Sci. 2011;42(11):3472-83.
23. Sun B, Fazeli F, Scott C, Yan X, Liu Z, Qin X, et al. Critical role of strain partitioning and deformation twinning on cracking phenomenon occurring during cold rolling of two duplex medium manganese steels. Scr Mater. 2017;130:49-53.
24. Malta PO, Dias FL, de Souza ACM, Santos DB. Microstructure and texture evolution of duplex stainless steels with different molybdenum contents. Mater Charact. 2018;142:406-21.
25. Li JS, Cheng GJ, Yen HW, Yang YL, Chang HY, Wu CY, et al. Microstrain and boundary misorientation evolution for recrystallized super DSS after deformation. Mater Chem Phys. 2020;246:122815.
26. Chen M, He J, Wang M, Li J, Xing S, Gui K, et al. Effects of deep cold rolling on the evolution of microstructure, microtexture, and mechanical properties of 2507 duplex stainless steel. Mater Sci Eng A. 2022;845:143224.
27. Dandekar TR, Khatirkar RK, Kumar A, Bibhanshu N, Suwas S. Unidirectional cold rolling of Fe-21Cr-5Mn-1.5Ni alloy – Microstructure, texture and magnetic properties. J Magn Magn Mater. 2022;549:169040.
28. Dandekar TR, Koya KSR, Chavhan J, Shah R, Khatirkar RK. Insights into the influence of cold rolling and accelerated isothermal aging on microstructure evolution, corrosion performance, σ precipitation and its kinetics in a low molybdenum Fe-21Cr-5Mn-1.5Ni alloy. Materialia (Oxf). 2023;30:101814.
29. Dandekar TR, Kumar A, Khatirkar RK, Kumar D, Suwas S. Effect of microstructure and texture on the evolution of mechanical properties in a cold rolled and annealed UNS S32101 lean duplex stainless steel sheet. Mater Chem Phys. 2023;299:127485.

30. Kumar A, Khatirkar RK, Chalapathi D, Kumar G, Suwas S. Microstructure and texture development during cold rolling in UNS S32205 and UNS S32760 duplex stainless steels. Metall Mater Trans, A Phys Metall Mater Sci. 2017;48(5):2349-62.
31. Kumar A, Khatirkar RK, Gupta A, Shekhawat SK, Suwas S. Deciphering the possible role of strain path on the evolution of microstructure, texture, and magnetic properties in a Fe-Cr-Ni alloy. Metall Mater Trans, A Phys Metall Mater Sci. 2018;49(8):3402-18.
32. Verbeken K, Barbé L, Raabe D. Evaluation of the crystallographic orientation relationships between FCC and BCC phases in TRIP steels. ISIJ Int. 2009;49(10):1601-9.
33. Alvi MH, Cheong SW, Weiland H, Rollett AD. Recrystallization and texture development in hot rolled 1050 aluminum. Mater Sci Forum. 2004;467-470:357-62.
34. Bracke L, Verbeken K, Kestens L, Penning J. Microstructure and texture evolution during cold rolling and annealing of a high Mn TWIP steel. Acta Mater. 2009;57(5):1512-24.
35. Lee K-M, Huh M-Y, Engler O. Quantitative analysis of micro-textures during recrystallization in an interstitial-free steel. Steel Res Int. 2012;83(9):919-26.
36. Badji R, Chauveau T, Bacroix B. Texture, misorientation and mechanical anisotropy in a deformed dual phase stainless steel weld joint. Mater Sci Eng A. 2013;575:94-103.
37. Wroński S, Tarasiuk J, Bacroix B, Baczmański A, Braham C. Investigation of plastic deformation heterogeneities in duplex steel by EBSD. Mater Charact. 2012;73:52-60.
38. Cullity BD, Stock SR. Elements of X-ray diffraction. 2nd ed. New Jersey: Prentice Hall; 2001. 531 p.
39. Stokes AR, Wilson AJC. The diffraction of X rays by distorted crystal aggregates - I. Proc Phys Soc. 1944;56(3):174-81.
40. Simon N, Krause M, Heinemann P, Erdle H, Böhlke T, Gibmeier J. Phase-specific strain hardening and load partitioning of cold rolled duplex stainless steel X2CrNiN23-4. Crystals. 2020;10(11):1-14.
41. Cullity BD, Graham CD. Introduction to magnetic materials. 2nd ed. New Jersey: John Wiley & Sons; 2009.
42. Martínez-de-Guerenu A, Arizti F, Díaz-Fuentes M, Gutiérrez I. Recovery during annealing in a cold rolled low carbon steel. Part I: kinetics and microstructural characterization. Acta Mater. 2004;52(12):3657-64.
43. Mitra A, Srivastava PK, De PK, Bhattacharya DK, Jiles DC. Ferromagnetic properties of deformation-induced martensite transformation in AISI 304 stainless steel. Metall Mater Trans, A Phys Metall Mater Sci. 2004;35A:599-605.
44. Sandim MJR, Souza Filho IR, Mota CFGS, Zilnyk KD, Sandim HRZ. Microstructural and magnetic characterization of a lean duplex steel: strain-induced martensite formation and austenite reversion. J Magn Magn Mater. 2021;517:167370.
45. Nohara K, Ono Y, Ohashi N. Composition and grain size dependencies of strain-induced martensitic transformation in metastable austenitic stainless steels. Tetsu To Hagane. 1977;63:777-82.
46. Masumura T, Fujino K, Tsuchiyama T, Takaki S, Kimura K. Effect of carbon and nitrogen on Md30 in metastable austenitic stainless steel. ISIJ Int. 2021;61(2):546-55.
47. Wright SI, Nowell MM. EBSD image quality mapping. Microsc Microanal. 2006;12(1):72-84.
48. Keichel J, Foct J, Gottstein G. Deformation and Annealing behavior of nitrogen alloyed duplex stainless steels. Part I: rolling. ISIJ Int. 2003;43(11):1781-7.